Electromagnetic induction in a fully 3-D anisotropic earth

Chester J. Weiss* and Gregory A. Newman*

ABSTRACT

The bulk electrical anisotropy of sedimentary formations is a macroscopic phenomenon which can result from the presence of porosity variations, laminated shaly sands, and water saturation. Accounting for its effect on induction log responses is an ongoing research problem for the well-logging community since these types of sedimentary structures have long been correlated with productive hydrocarbon reservoirs such as the Jurassic Norphlet Sandstone and Permian Rotliegendes Sandstone. Presented here is a staggered-grid finite-difference method for simulating electromagnetic (EM) induction in a fully 3-D anisotropic medium. The electrical conductivity of the formation is represented as a full 3×3 tensor whose elements can vary arbitrarily with position throughout the formation. To demonstrate the validity of this approach, finite-difference results are compared against analytic and quasi-analytic solutions for tractable 1-D and 3-D model geometries. As a final example, we simulate 2C–40 induction tool responses in a crossbedded aeolian sandstone to illustrate the magnitude of the challenge faced by interpreters when electrical anisotropy is neglected.

INTRODUCTION

Detection of the electrical anisotropy of geologic formations is a problem that has attracted the attention of geophysicists for nearly 70 years (see Maillet and Doll, 1932; Kunz and Moran, 1958). The motivation has varied greatly, ranging from groundwater investigation (Christensen, 2000) to hydrocarbon exploration (Moran and Gianzero, 1979; Anderson et al., 1998; Kriegshäuser et al., 2000) to regional-scale lithospheric mapping (Weidelt, 1999; Everett and Constable, 1999). Some materials, such as single crystal olivine, exhibit an inherent electrical anisotropy (Constable et al., 1992). Other materials, such as clastic sedimentary reservoir rock, exhibit an electrical anisotropy that is a macroscopic effect as a result of small-scale petrophysical variations (see Anderson et al., 1994).

The petrophysical origins of macroscopic electrical anisotropy in hydrocarbon reservoirs can be generally classified into three categories. The first of these is anisotropy from variations in water saturation. For example, in crossbedded sandstones (Figure 1), the variations in grain size and porespace geometry result in a graded water saturation profile across strata within a stratigraphic set. The variable electrical conductivity contrast between the grains and the pore space result in a macroscopic electrical anisotropy (Klein et al. 1997) in which the conductivity in the direction perpendicular to the set is less than the conductivity in the plane of the set. The second mechanism arises from thin interbeds of sediments with different electrical properties. Among others who have investigated this mechanism, Klein et al. (1997) show that the high-conductivity contrast between shales and sands results in a pronounced anisotropy for shaly sand sequences. Last, porosity variations have recently been identified as a potential source of electrical anisotropy in uniformly saturated water sands (Schön et al., 2000).

The presence of electrical anisotropy has long been recognized as a potentially significant source of error in traditional induction log analysis (e.g., Klein, 1993). A critical component in understanding this problem is the ability to accurately predict the behavior of induced EM fields in anisotropic media. To this end, we have developed a numerical algorithm that computes the electric and magnetic fields resulting from an inductive source embedded in a fully 3-D generalized anisotropic medium. The generalized anisotropy of the medium is described by a symmetric 3×3 anisotropy tensor. In our algorithm, we use an edge-centered, staggered-grid, finite-difference solution to Maxwell's equations in the quasi-static limit. One benefit from this modeling algorithm for the log analyst is the ability to better predict the response of complex 3-D formation geometries and to quantify the magnitude of the interpretation error when anisotropy is neglected.

Some attempts at 3-D modeling of anisotropic media simplify the algorithmic complexity by considering a formation conductivity described by a diagonal 3×3 conductivity tensor. Under this assumption, an integral equation solution (Graciet and Shen, 1998) and a finite difference solution (Newman and Alumbaugh, 2002) were developed to simulate induction log response in 3-D formations with the caveat that the principal axes of the anisotropy tensor were uniformly constrained to the x-y-z–directions in the modeling domain. This restriction eliminated the possibility of modeling, for example, a crossbedded aeolian sandstones (Figure 1).

Other formulations of the generalized 3-D anisotropy problem include those of Davydycheva and Druskin (1999) and Weidelt (1999). These, along with our study, are based on the finite difference staggered grid where electric and magnetic fields are sampled at different points on a Cartesian mesh. Davydycheva and Druskin (1999) utilize a variant known as Lebedev's grid, where all components of the electric field are sampled at each node of a one grid and all components of the magnetic field are sampled at each node of a second (staggered) grid. This avoids the spatial conductivity averaging schemes that typically arise in finite difference methodologies, including the one present here, but has the disadvantage that the anisotropy problem requires a fourfold increase in computer storage requirements when compared with a similar isotropic problem. As an alternative, Weidelt (1999) presents a formulation based upon a face-centered discretization of the governing partial differential equation (PDE), discretized using only components of the electric field vector which are normal to and located at the centers of cell faces. In contrast, our edge-based approach uses only electric field components that are tangential to conductivity boundaries and are thus locally continuous and well behaved. This difference between our formulation and Weidelt's (1999) results in significant differences in how electrical conductivity is approximated at electric field points. Our method is straightforward volume averaging, in contrast to the relatively complex arrangement of arithmetic and harmonic averages proposed by Weidelt.
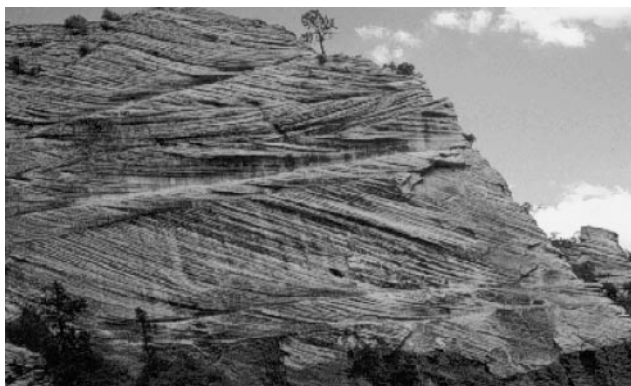

FIG. 1. Crossbedded aeolian deposits in the Jurassic Navajo Sandstone from Zion National Park, Utah. Macroscopic electrical anisotropy in this formation results from small-scale variations in grain size and pore space (from depositional kinematics), which also give rise to the differential weathering shown here. This formation is analogous to the Permian Rotliegendes and Jurassic Norphlet Sandstones, classic reservoirs of the North Sea and the Gulf of Mexico, respectively. Photo courtesy of Duncan Huron, Duke University.

The paper is organized as follows. We begin by deriving the governing PDE which describes low-frequency electromagnetic (EM) induction in anisotropic media. Next, we introduce the finite difference method for staggered grids used in solving the governing PDE. Incorporating a fully generalized anisotropy tensor into the finite difference method is discussed in the text; however, a detailed presentation of the finite difference system of equations is deferred to the Appendix. In closing the discussion of the finite difference method, we briefly comment on the quasi-minimal residual method to solve the finite difference linear system of equations. Last, we present the results of several numerical experiments. The first set of results illustrates the agreement between the finite difference, integral-equation, and quasi-analytic solutions for 1-D and 3-D problems. The last set of computations illustrates the magnitude of the effect of anisotropy on the response of a 2C–40 induction logging instrument in a fully 3-D crossbedded formation.

METHODOLOGY

The governing equations for EM induction are Faraday's law,

$$\nabla \times \mathbf{E} = -i\omega\mathbf{B}, \qquad (1)$$

which relates the electric field $\mathbf{E}$ to magnetic induction $\mathbf{B}$, and Ampere's law,

$$\nabla \times \mathbf{H} = \mathbf{J}_i + \mathbf{J}_s + i\omega\mathbf{D}, \qquad (2)$$

which relates the magnetic field $\mathbf{H}$ to the induced and source current densities ($\mathbf{J}_i$ and $\mathbf{J}_s$) and displacement fields $\mathbf{D}$. An $\exp(i\omega t)$ time dependence is implied, where ω is angular frequency.

The induction and magnetic fields are related by the constitutive relationship $\mathbf{B} = \mu\mathbf{H}$, where μ is the magnetic permeability of the medium, chosen here to be that of free space, $\mu = \mu_0 = 4\pi \times 10^{-7}$ H/m. Similarly, the displacement and electric fields are assumed to be related by $\mathbf{D} = \epsilon\mathbf{E}$, where ϵ is the electric permittivity. Last, the induced current density $\mathbf{J}_i$ is assumed to be from purely ohmic conduction in an anisotropic medium, written as

$$\mathbf{J}_i = \bar{\sigma}\mathbf{E}, \qquad (3)$$

where $\bar{\sigma}$ is a symmetric 3×3 tensor. The symmetry of the conductivity tensor results from neglecting the effect of Hall currents (Onsager, 1931) and is necessary for physically sensible energy dissipation within the earth.

In formulating the EM induction problem, $\mathbf{E}$ can be expressed as the sum of a primary contribution $\mathbf{E}_0$ from $\mathbf{J}_s$ embedded in a background reference medium and a scattered contribution $\mathbf{E}'$ arising from conductivity and permittivity variations which deviate from the background structure. That is,

$$\mathbf{E} = \mathbf{E}_0 + \mathbf{E}', \qquad (4)$$

where the background structure is chosen to be easy to evaluate. For simplicity, we choose the background electrical structure to be a uniform whole space of conductivity σ_0 and permittivity ϵ_0. Formulating the problem in terms of scattered fields is desirable because the computations are more robust and accurate, particularly near the source and for the in-phase fields (Newman and Alumbaugh, 2002). Thus, combining

equations (1)–(4) yields a single, second. order PDE in terms of the scattered electric field:

$$\nabla \times \nabla \times \mathbf{E}' + i\omega\mu_0(\bar{\sigma} + i\omega\epsilon)\mathbf{E}' = -i\omega\mu_0\mathbf{J}_0. \quad (5)$$

The term $\mathbf{J}_0$ is the effective source current density for the scattered fields,

$$\mathbf{J}_0 = [(\bar{\sigma}(\mathbf{x}) - \sigma_0\mathbf{I}) + i\omega(\epsilon(\mathbf{x}) - \epsilon_0)\mathbf{I}]\,\mathbf{E}_0, \quad (6)$$

where the spatial dependence of the conductivity and permittivity is explicitly noted by the position vector $\mathbf{x}$ and where $\mathbf{I}$ is the 3×3 identity matrix. For the induction logging calculations presented later in the Examples section, the fields are computed in the low-frequency limit ($\sigma \gg \omega\epsilon$). This approximation is reasonable since the permittivity of the formation yields a negligible effect at frequencies up to $f = \omega/2\pi \sim 1$ MHz. Nonetheless, the permittivity terms are retained in equations (5) and (6) for completeness and to emphasize that the approach taken here also applies to higher frequency problems (see Newman and Alumbaugh, 1999).

The unknown fields $\mathbf{E}'$ in equation (5) are determined by the method of finite differences on a staggered Yee grid (Yee, 1966) where the physical domain is discretized into Cartesian cells and the scattered electric field components (E'_x, E'_y, and E'_z) are defined on the edges of the cells. Coordinates of the nodes which define cell corners are represented by indicial notation as (i, j, k), representing the point $\mathbf{x} = x_i\hat{x} + y_j\hat{y} + z_k\hat{z}$. If necessary, magnetic fields can be computed at cell faces as a postprocessing step based on a difference approximation to Faraday's law [equation (1)]. Figure 2 illustrates the relationship between a cell and the computed electric field components.

Figure 2 indicates conductivity is required on cell edges because that is where the electric field is sampled. In the time domain, Wang and Hohmann (1993) demonstrate that the average isotropic conductivity on each cell edge can be evaluated using Ampere's law by tracing a line integral of the magnetic field, centered on the midpoint of the cell edge. The resulting conductivity is a weighted sum of the conductivities of the four adjoining cells, where the weighting is based on the area of each
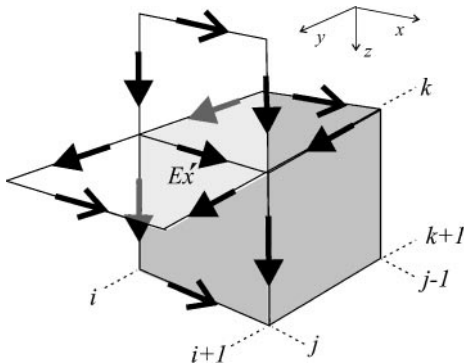

FIG. 2. The staggered-grid stencil used for the finite difference computations. Discretization of the $\nabla \times \nabla\times$ operator for the $\hat{x}$-component of equation (5) at point $(i + 1/2, j, k)$ utilizes components of $\mathbf{E}'$ from each of the 13 locations indicated by the arrows. A subset of nine $\mathbf{E}'$ components, indicated by solid arrowheads, is used for discretization of the $\bar{\sigma}\mathbf{E}'$ term. Also shown is a model cell throughout which the electrical conductivity tensor remains constant.

cell that is bounded by this line integral. This spatial averaging approach has been successfully applied to frequency-domain modeling (Newman and Alumbaugh, 1995). For the anisotropy problem, however, the approach is inadequate because evaluating the current density term in equation (5) requires values of not only the $\hat{x}$-component of the scattered electric field at the point $(i + 1/2, j, k)$ but also the $\hat{y}$- and $\hat{z}$-components at this same point, since in the continuous case

$$\hat{x} \cdot \bar{\sigma}\mathbf{E}' = \sigma_{xx}E'_x + \sigma_{xy}E'_y + \sigma_{xz}E'_z. \quad (7)$$

The $\sigma_{xx}E'$ term is treated in a fashion similar to the isotropic case, being approximated by a weighted average of cell conductivities for the four cells adjacent to the point $(i + 1/2, j, k)$, where the averaging volume Ω is given by the region $x_i < x < x_{i+1}$, $y_{j-1/2} < y < y_{j+1/2}$ and $z_{k-1/2} < z < z_{k+1/2}$. Yet, because E'_y and E'_z are not defined in the staggered Yee grid at these points (see Figure 2), we are motivated to seek an estimate of their values instead. To determine such an estimate, we begin with the following definitions:

$$\langle \sigma_{xy}E'_y \rangle \overset{\text{def}}{=} \frac{1}{\Omega} \int_\Omega \sigma_{xy}E'_y \, dV$$

and

$$\langle \sigma_{xz}E'_z \rangle \overset{\text{def}}{=} \frac{1}{\Omega} \int_\Omega \sigma_{xz}E'_z \, dV, \quad (8)$$

where the brackets indicate spatial averaging. (A similar expression can be written for the $\sigma_{xx}E'_x$ term. But since the E'_x component is tangential to any possible conductivity jumps in the region Ω, the expression simplifies to the simple volume weighting already described.) Because the E'_y and E'_z field components can be discontinuous across the xz-plane at y_j and the xy-plane at z_k, respectively, we evaluate the integrals in equation (8) piecewise over Ω. Once the integrals are evaluated, they are substituted into equation (5) as approximate values for the $\sigma_{xy}E'_y$ and $\sigma_{xz}E'_z$ terms. For the points $(i + 1/2, j, k)$ mentioned above, explicit expressions for these two integrals are given by

$$\langle \sigma_{xy}E'_y \rangle \simeq \frac{1}{\Omega^x_{i,j,k}} \left\{ \frac{1}{2}\left[E'_y\left(i, j - \frac{1}{2}, k\right) \right.\right.$$
$$\left. + E'_y\left(i+1, j - \frac{1}{2}, k\right) \right]\tilde{\sigma}_{xy}\left(i + \frac{1}{2}, j - \frac{1}{2}, k\right)$$
$$+ \frac{1}{2}\left[E'_y\left(i, j + \frac{1}{2}, k\right) + E'_y\left(i+1, j + \frac{1}{2}, k\right) \right]$$
$$\left. \times \tilde{\sigma}_{xy}\left(i + \frac{1}{2}, j + \frac{1}{2}, k\right) \right\} \quad (9)$$

and

$$\langle \sigma_{xz}E'_z \rangle \simeq \frac{1}{\Omega^x_{i,j,k}} \left\{ \frac{1}{2}\left[E'_z\left(i, j, k - \frac{1}{2}\right) \right.\right.$$
$$\left. + E'_z\left(i+1, j, k - \frac{1}{2}\right) \right]\tilde{\sigma}_{xz}\left(i + \frac{1}{2}, j, k - \frac{1}{2}\right)$$
$$+ \frac{1}{2}\left[E'_z\left(i, j, k + \frac{1}{2}\right) + E'_z\left(i+1, j, k + \frac{1}{2}\right) \right]$$
$$\left. \times \tilde{\sigma}_{xz}\left(i + \frac{1}{2}, j, k + \frac{1}{2}\right) \right\}. \quad (10)$$

The terms $\tilde{\sigma}_{xy}$ and $\tilde{\sigma}_{xz}$ are given by

$$\tilde{\sigma}_{xy}\left(\alpha + \frac{1}{2}, \beta + \frac{1}{2}, \gamma\right)$$
$$= \Delta_{\alpha}^{x}\left(\frac{1}{2}\Delta_{\beta}^{y}\right)\left(\frac{1}{2}\Delta_{\gamma-1}^{z}\sigma_{xy}^{[\alpha,\beta,\gamma-1]} + \frac{1}{2}\Delta_{\gamma}^{z}\sigma_{xy}^{[\alpha,\beta,\gamma]}\right) \quad (11)$$

and

$$\tilde{\sigma}_{xz}\left(\alpha + \frac{1}{2}, \beta, \gamma + \frac{1}{2}\right)$$
$$= \Delta_{\alpha}^{x}\left(\frac{1}{2}\Delta_{\gamma}^{z}\right)\left(\frac{1}{2}\Delta_{\beta-1}^{y}\sigma_{xz}^{[\alpha,\beta-1,\gamma]} + \frac{1}{2}\Delta_{\beta}^{y}\sigma_{xz}^{[\alpha,\beta,\gamma]}\right), \quad (12)$$

where the distances between neighboring cells in x, y, and z are denoted as $\Delta_{\alpha}^{x} = x_{\alpha+1} - x_{\alpha}$, $\Delta_{\beta}^{y} = y_{\beta+1} - y_{\beta}$, and $\Delta_{\gamma}^{z} = z_{\gamma+1} - z_{\gamma}$, respectively. Consequently, the averaging volume $\Omega_{i,j,k}^{x}$ in equations (9) and (10) is given by $\Delta_{i}^{x}\Delta_{j-\frac{1}{2}}^{y}\Delta_{k-\frac{1}{2}}^{z}$, where the superscript x on Ω indicates that the averaging volume is centered on x-directed cell edges. Furthermore, the superscript $[\alpha, \beta, \gamma]$ on σ_{xy} and σ_{xz} indicates that the conductivity value is that of the cell defined by the region $x_{\alpha} < x < x_{\alpha+1}$, $y_{\beta} < y < y_{\beta+1}$, and $z_{\gamma} < z < z_{\gamma+1}$. To complete the discretization of equation (5), the remaining current density terms $\hat{y} \cdot \bar{\sigma}\mathbf{E}'$ and $\hat{z} \cdot \bar{\sigma}\mathbf{E}'$ can easily be derived using techniques similar to those shown for the $\hat{x} \cdot \bar{\sigma}\mathbf{E}'$ term.

Inspection of equations (9) and (10) suggests this formulation may be interpreted as a variant of the face-centered approach of Weidelt (1999) since, for example, the term $\frac{1}{2}(E_{y}'(i, j - 1/2, k) + E_{y}'(i + 1, j - 1/2, k))$ is approximately equal to $E_{y}'(i + 1/2, j - 1/2, k)$, an electric field component centered at a finite difference cell face but tangent to that cell face. The formulation, however, remains edge centered because equation (5) is discretized only in terms of electric field components located along the midpoints of cell edges and tangent to those edges. A further distinction between the face-centered approach and the interpretation posed above is that the face-centered approach uses electric field components normal to the cell face. In contrast to equations (11) and (12), the face-centered approach leads to a cumbersome arrangement of harmonic and arithmetic averages to arrive at a reasonable approximation to the current density term in equation (5). The differences in algorithmic complexity can be traced, in part, to the fact the edge-centered approach uses electric field components at locations within the finite difference mesh, where they are generally well defined and continuous, whereas the face-centered approach does not.

For brevity, explicit formulas for the system of equations arising from the finite difference discretization of equation (5) are contained in the Appendix. There, we find the vector of unknown scattered electric field components $\mathbf{y}$ is related to the the vector $\mathbf{b}$ of volume-scaled source terms $\mathbf{J}_{0}$ by the linear system of equations

$$\mathbf{Ay} = \mathbf{b}, \quad (13)$$

where $\mathbf{A}$ is a complex symmetric coefficient matrix. It is derived from scaling equations (A-1)–(A-3) and applying a homogeneous Dirichlet condition to scattered electric field components on the outermost boundary of the finite-difference mesh. This system is solved efficiently by the quasi-minimal resid-

ual (QMR) iterative method for complex symmetric matrices (Freund, 1992). Iterative matrix solvers are available for a symmetric complex matrices (e.g., Freund, 1993), but they require twice as many matrix–vector products per iterative step as their symmetric counterpart. Because much of the computational cost for each QMR iterate is generated by the matrix–vector product, the straightforward symmetrization procedure produced by scaling can significantly minimize the time required to obtain a solution. We also implement a Jacobi preconditioner to further reduce the computational time and to improve the stability of the convergence sequence. Future work in this area includes implementation of the low induction number (LIN) preconditioner (Newman and Alumbaugh, 2001), which can reduce computational time by as much as a factor of 10 for isotropic media.

EXAMPLES

As a way to simplify the construction of a geologically sensible conductivity model, we choose to describe the electrical conductivity tensor in terms of values in a principal axes reference frame and then describe the reference frame orientation via Euler angles. In layered sedimentary formations, for example, the tensor is described compactly as $\bar{\sigma} = \text{diag}(\sigma_{\parallel}, \sigma_{\parallel}, \sigma_{\perp})$, where $\sigma_{\parallel}$ is the conductivity in the bed-parallel direction and $\sigma_{\perp}$ is the conductivity perpendicular to the bedding planes. The conductivity tensor is transformed from the position-dependent principal axes reference frame to the x, y, and z axes by multiplication with a rotation matrix $\mathbf{R}$,

$$\bar{\sigma} = \mathbf{R}^{T}\text{diag}(\sigma_{\parallel}, \sigma_{\parallel}, \sigma_{\perp})\mathbf{R}, \quad (14)$$

where T denotes the transpose operator. The elements of $\mathbf{R}$ are the direction cosines between the principal axes and the x-y-z reference frame. When the conductivity in two of the three principal directions is equal, each of the six direction cosines is uniquely expressed in terms of only two Euler angles corresponding to the strike ϕ and dip θ of the laminations (Figure 3). This brings the total number of model parameters for each model cell in Figure 2 to four: $\sigma_{\perp}$, $\sigma_{\parallel}$, θ, and ϕ. The
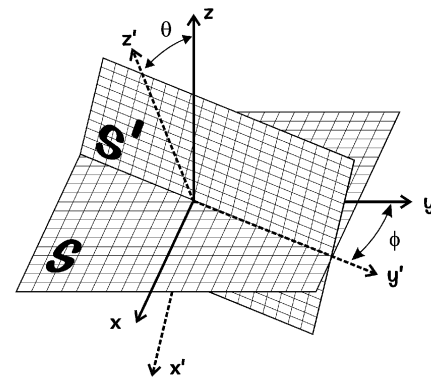

FIG. 3. Geometric relationship between the model reference frame (x, y, z) and the principal axes reference frame (x', y', z'). The plane labeled S intersects the origin and is perpendicular to the z axis. The plane labeled S', representing the bedding planes, intersects the origin and is perpendicular to the z' axis. Angles ϕ and θ represent the strike and dip of the plane S' with respect to the plane S. For the particular rotations shown in the figure, $\phi < 0$ by convention.

rotation matrix then takes the form

$$\mathbf{R}^T = \begin{pmatrix} \cos\theta\,\cos\phi & -\sin\phi & \sin\theta\,\cos\phi \\ \cos\theta\,\sin\phi & \cos\phi & \sin\theta\,\sin\phi \\ -\sin\theta & 0 & \cos\theta \end{pmatrix}. \quad (15)$$

Note that the orientation of the principal axes, and therefore the values within the rotation matrix in equations (14) and (15), can vary as a function of position within the conducting formation.

To demonstrate the validity of the finite difference scheme, we first present results of an internal consistency check and then additional results from comparisons with previously developed quasi-analytic solutions. The internal consistency check is based upon the computation of magnetic fields form a magnetic dipole source oriented 45° with respect to the principal axes of a uniform whole space (Figure 4). One solution was obtained when the principal axes were aligned with the x-y-z reference frame and the source was tilted 45°. The other was obtained by tilting the principal axes and aligning the source in the z-direction. For these and all models that follow, the background conductivity model is taken as a uniform isotropic whole space of conductivity $\sigma_\parallel$. While the effect of the borehole conductivity was not included in this model, the borehole–axial magnetic fields were computed for a sequence of source–receiver offsets and showed favorable comparison (Figure 5). Results for the first of these models, where the source was tilted, were generated by superposition of the fields form an x-directed source and fields from a z-directed one. Thus, this comparison is a more stringent test than it may at first appear, since numerical error is compounded by summing the fields for the x and z sources; yet the agreement between the two models is quite acceptable.

The first check of finite difference algorithm with an independently derived solution computes the borehole effects on the same coaxial transmitter–receiver array examined by the internal consistency check discussed above (Figure 6). Comparing the finite difference with a 3-D integral equation solution (Avdeev et al., 2002) demonstrates favorable agreement (Figure 7), especially for imaginary fields from which apparent conductivity values can derived (Moran and Kunz, 1962). The

origin of the slight difference (only a few percent) between the real component of the fields, however, is unclear. Also shown is the finite difference solution in the absence of the conducting borehole, verifying the well-established fact that the borehole effect decreases with increased source–receiver offsets.
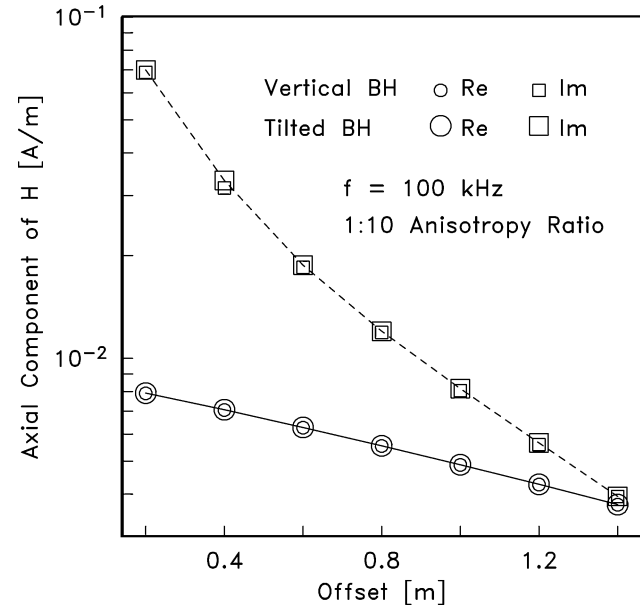
FIG. 5. Axial component of the finite difference-computed magnetic field from evaluating the models shown in Figure 4. The quantity plotted is the difference between the total field and the field attributable to an equivalent source located in a vacuum.

FIG. 6. Schematic of a deviated borehole in an anisotropic formation. The 45° deviation is constrained to the xz-plane. The transmitter (Tx) and receiver (Rx) arrays are coaxial loops centered on the borehole axis, and each separated by 0.2 m. Borehole conductivity is $\sigma_b = 10$ S/m. Anisotropic formation conductivities are $\sigma_{xx} = \sigma_{yy} = 1.0$ S/m and $\sigma_{zz} = 0.25$ S/m.
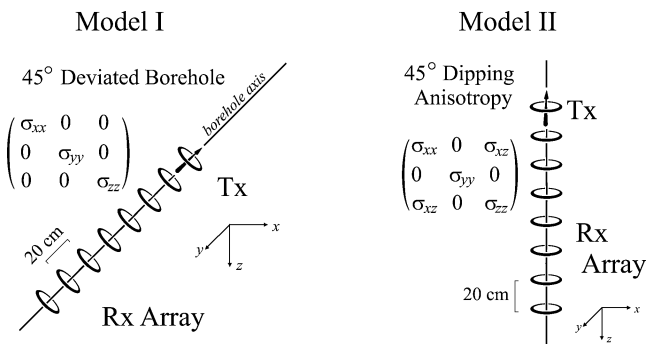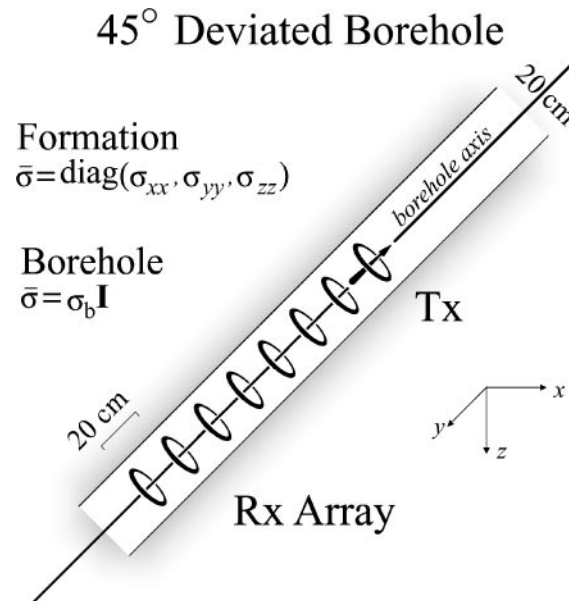

FIG. 4. Schematic representation of two models constructed for an internal consistency check of the finite difference solutions. Shown are the receiver (Rx) coil spacing, finite difference reference frame, and formation conductivity tensor for each of the two models. The conductivity tensor of the formation is given by equation (12), where $\sigma_\perp = 0.1$ S/m and $\sigma_\parallel = 1.0$ S/m. The transmitter (Tx) frequency is 100 kHz.

The second check of the finite difference algorithm with an independently derived solution is based upon computing synthetic induction logs for a 2C–40 sonde (one receiver coil coaxial with a 20-kHz transmitting coil, offset by 1.016 m) traversing the contact between an isotropic upper half-space and an anisotropic lower half-space. Within Figures 8a–c are results for three different conductivity models, comparing the finite difference solution at three different discretizations with that of Anderson et al. (1998), which is a quasi-analytic solution. The models differ from one another in the amount of dip within the lower half-space: 0°, 60°, and 90°. Clearly, as the discretization is made finer, the finite difference solutions converge toward quasi-analytic solutions.

Three different finite difference meshes were examined to test the convergence of the finite difference solution to the Anderson et al. (1998) solution. The physical domain of the model space was a 15-m cube centered on the bed contact. Node spacing in the vertical direction was geometrically distributed, allowing for small values near the bed contact, with a 10% increase in successive node intervals as a function of distance from the contact. Lateral node spacing was kept uniform. As expected, the finite difference solution converges to the Anderson et al. (1998) solution as the number of mesh points is increased, resulting in acceptable agreement for modest-sized finite difference meshes. For the nine different finite difference curves shown in Figures 8a–c, the time required to compute one logging point on a 500-MHz DS-20 Alpha workstation ranges from ∼23 to ∼1300 s (Table 1), depending generally on the mesh size and the dip of anisotropy in the lower half-space.

As an example of an application of our finite difference anisotropy modeling code, we consider the case of a borehole induction tool in a crossbedded sandstone unit. Aeolian-deposited crossbedded sands have long been identified as candidate reservoir rocks (e.g., the Jurassic Norphlet Sandstone
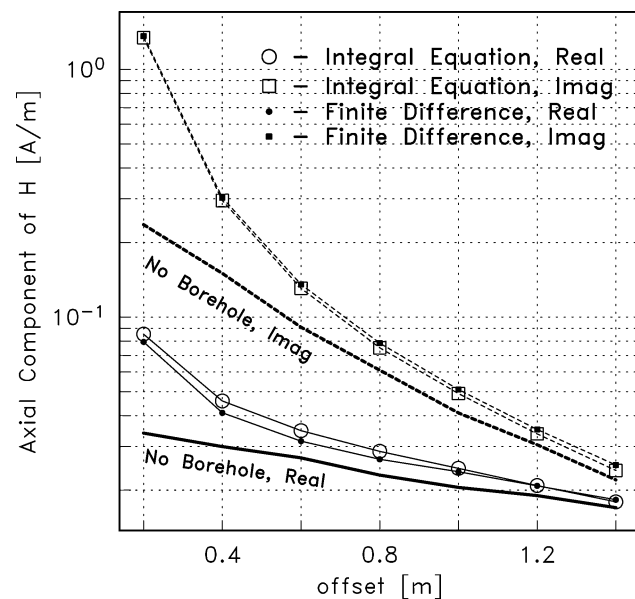

FIG. 7. Comparison of finite difference and integral equation solutions for a magnetic field along the axis of a 45° dipping borehole resulting from an axially aligned 160-kHz magnetic dipole. The quantity plotted is the difference between the total field and the field form equivalent source located in a vacuum.

and Permian Rotliegendes Sandstone) and remain targets for hydrocarbon exploration (Berg, 1986). Our modeling results simulate the repose of a 2C–40 borehole induction tool crossing a bed boundary in a conductive sandstone and demonstrate the effects of electrical anisotropy on the apparent conductivity curves inferred from this instrument.

Two classes of sedimentary structures were evaluated with the modeling software: symmetrically dipping herringbone crossbeds and asymmetrically dipping crossbeds. Figure 9 illustrates the geometric configuration for the symmetrically dipping case where the borehole axis intersects the bed boundary at 90°. This borehole configuration is not a limitation of the modeling software. Rather, it is a decision intended to isolate the effects of the formation anisotropy from dipping borehole effects. For each of the models, we set the conductivity values of the sand unit as $\sigma_\perp = 0.1$ S/m and $\sigma_\parallel = 1.0$ S/m. The high-conductivity ratio of 1:10 is consistent with that seen in clean saturated sands (Klein et al., 1997). Our finite difference solution can incorporate the effects of the borehole in the tool response (see Figures 6 and 7). However, to further isolate the effects of formation anisotropy, the conductivity of the borehole and drilling mud were not included in the simulations.

Shown in Figures 10 and 11 are the simulated apparent resistivity curves as the 2C–40 tool traverses a bed boundary within the sand unit. Owing to the high conductivity of the formation, the apparent resistivity curves were skin effect boosted according to standard industry practice. Simply stated, the process incorporates higher-order terms into the approximately linear mapping between apparent conductivity and receiver signal strength (Moran and Kunz, 1962). Furthermore, in the limit of large values for the anisotropy ratio $\lambda^2 = \sigma_\parallel/\sigma_\perp$, the well-known formula for apparent conductivity σ_a given by Moran and Gianzero (1979),

$$\sigma_a = \sigma_\perp \lambda \sqrt{\lambda^2 \cos^2 \theta + \sin^2 \theta}, \qquad (16)$$

can be simplified to read $\sigma_a \simeq \sigma_\parallel \cos \theta$. If the dip of the formation with respect to the borehole axis is known, perhaps through conventional dipmeter data, then an estimate of $\sigma_\parallel$ is easily obtained with a coaxial induction sonde if it is reasonable to assume that λ^2 is large. For the examples shown in Figures 10 and 11, $\lambda^2 = 10$. It is clear that away from the effects of the bed boundary at $z = 0$, the value of $\sigma_a/\cos \theta$ for various dip angles θ is close to 1.0 S/m, the actual value of $\sigma_\parallel$.

CONCLUSIONS

When combined with a physically tenable petrophysical model, 3-D induction modeling capabilities have the potential to reduce the uncertainty in induction log interpretation. Clearly, the characterization of reservoir properties with induction logs cannot be improved if either the constitutive relationship between petrophysical parameters is poorly understood or if the induction modeling software cannot simulate relevant geologic structures. Contributing to the latter effort serves as the motivation for our study.

For example, the what-if scenarios presented for aeolian sands illustrate the complexity that electrical anisotropy can introduce in the induction log response curves. The anomalous behavior at the bed boundary is entirely the result of a change in the orientation of the principal axes, not a change in the conductivity values. An unsuspecting log analyst could

a)

0 deg dipping lower halfspace

b)

60 deg dipping lower halfspace
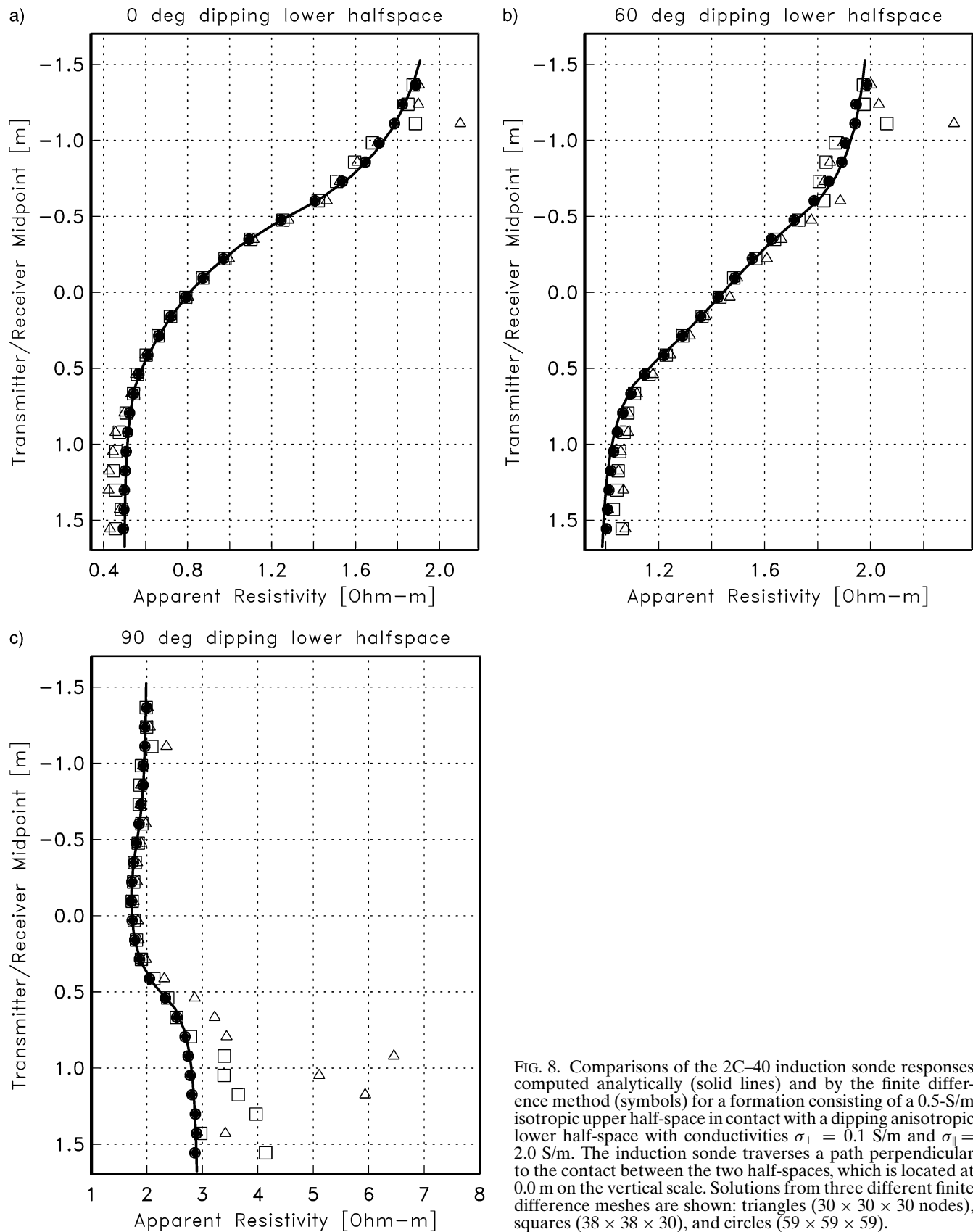
c)

90 deg dipping lower halfspace

FIG. 8. Comparisons of the 2C–40 induction sonde responses computed analytically (solid lines) and by the finite difference method (symbols) for a formation consisting of a 0.5-S/m isotropic upper half-space in contact with a dipping anisotropic lower half-space with conductivities $\sigma_\perp = 0.1$ S/m and $\sigma_\parallel = 2.0$ S/m. The induction sonde traverses a path perpendicular to the contact between the two half-spaces, which is located at 0.0 m on the vertical scale. Solutions from three different finite difference meshes are shown: triangles ($30 \times 30 \times 30$ nodes), squares ($38 \times 38 \times 30$), and circles ($59 \times 59 \times 59$).

Table 1. Summary of model parameters and quasi-minimal residual (QMR) performance for the synthetic induction logs shown in Figure 8. Times, iteration counts, and rates are average values to compute one logging point for each of the models evaluated. Model size is indicated by the number of finite difference mesh nodes N_x, N_y, and N_z in the x-, y-, and z-directions, respectively. Imposing the Dirichlet boundary condition on tangential $\mathbf{E}'$ results in a linear system with $3N_xN_yN_z - 5(N_xN_y + N_xN_z + N_yN_z) + 8(N_x + N_y + N_z) - 12$ unknowns. The QMR iterative sequence terminated at a normalized residual of $\|\mathbf{Ay}_i - \mathbf{b}\|_2/\|\mathbf{b}\|_2 = 4 \times 10^{-7}$.

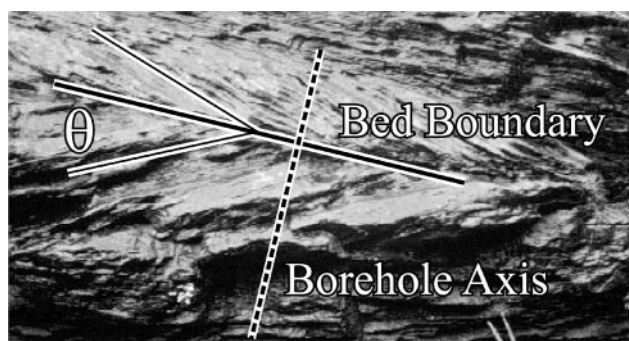|		QMR performance			
Dip (°)	$N_x \times N_y \times N_z$	Unknowns	Iterations	Time (s)	Time/it. (s)
0	$30 \times 30 \times 30$	68 208	316	22.6	0.0709
0	$38 \times 38 \times 30$	112 176	720	105	0.145
0	$59 \times 59 \times 59$	565 326	625	492	0.787
60	$30 \times 30 \times 30$	68 208	548	46.6	0.0851
60	$38 \times 38 \times 30$	112 176	997	142	0.142
60	$59 \times 59 \times 59$	565 326	1164	913	0.781
90	$30 \times 30 \times 30$	68 208	530	44.2	0.0833
90	$38 \times 38 \times 30$	112 176	940	134	0.143
90	$59 \times 59 \times 59$	565 326	1755	1260	0.732

FIG. 9. Photograph of a crossbedded sandstone with symmetric laminations dipping at an angle θ with respect to the bed boundary. Also shown is the orientation (normal to the bed boundary) of the borehole axis considered in the numerical simulations. Photo courtesy of Duncan Huron, Duke University.

reasonably argue that the anomaly represents a separate lithologic unit. Furthermore, our results concur with those of Moran and Gianzero (1979), showing that inadequate knowledge of formation dip could lead to an anomalous baseline shift in the resistivity value, which could lead to mischaracterization of entire bed sets (Figures 10 and 11).

In summary, our algorithm for modeling EM induction in an anisotropic medium represents a technical advance in the ability to accurately simulate the effects of geologic structures on induction tool response. It uses the finite difference method to arrive at a complex symmetric system of linear equations which are solved efficiently for the scattered electric fields by fast Krylov subspace methods. The work differs from other 3-D modeling efforts in the details of the field discretization and the method for computing volume-averaged electrical properties. It offers the advantages that volume averaging is relatively straightforward and the computational burden of the anisotropic problem is not significantly greater than that of a similar isotropic problem.

ACKNOWLEDGMENTS

REFERENCES

Anderson, B. I., Barber, T. D., and Gianzero, S. C., 1998, The effect of crossbedding anisotropy on induction tool response: 39th Logging Symposium, Soc. Prof. Well Log Anal., Expanded Abstracts, Paper B.
Anderson, B., Bryant, I., Lülig, M., Spies, B., and Helbig, K., 1994, Oilfield anisotropy: Its origins electrical characteristics: Oilfield Rev., **6**, 48–56.
Avdeev, D. B., Kuvshinov, A. V., Pankratov, O. V., and Newman, G. A., 2002, Three-dimensional induction logging problems, part I: An integral equation solution and model comparisions: Geophysics, **67**, 413–426.
Berg, R. R., 1986, Reservoir sandstones: Prentice-Hall Inc.
Christensen, N. B., 2000, Difficulties in determining electrical anisotropy in subsurface investigations: Geophys. Prosp., **48** 1–19.
Constable, S., Shankland, T. J., and Duba, A., 1992, The electrical conductivity of an isotropic olivine mantle: J. Geophys. Res., **97**, 3397–3404.
Davydycheva, S., and Druskin, V., 1999, Staggered grid for Maxwell's equations in 3-D anisotropic media, *in* Oristaglio, M., and Spies, B., Eds., Three-dimensional electromagnetics: Soc. Expl. Geophys., 119–137.
Everett, M. E., and Constable, S., 1999, Electric dipole fields over an anisotropic seafloor: Theory and application to the structure of 40 Ma Pacific Ocean lithosphere: Geophys. J. Internat., **136**, 41–56.
Freund, R. W., 1992, Conjugate gradient-type methods for linear systems with complex symmetric coefficient matrices: SIAM J. Sci. Stat. Comput., **13**, 425–448.
——— 1993, A transpose-free quasi-minimal residual algorithm for non-Hermitian linear systems: SIAM J. Sci. Stat. Comput., **14**, 470–482.
Graciet, S., and Shen, L. C., 1998, Theory and numerical simulation of induction and MWD resistivity tools in anisotropic dipping beds: The Log Analyst, **38**, 24–37.
Klein, J. D., 1993, Induction log anisotropy corrections: The Log Analyst, **34**, 18–27.
Klein, J. D., Martin, P. R., and Allen, D. F., 1997, The petrophysics of electrically anisotropic reservoirs: The Log Analyst, **38**, 25–36.
Kriegshäuser, B., Fanini, O., Forgang, S., Mollison, R., Yu, L., Gutpta, P., Koelman, J. M. V., and van Popta, J., 2000, Increased oil-in-place in low resistivity reservoirs from multi-component induction log data: 41st Logging Symposium, Soc. Prof. Well Log Anal., Expanded Abstracts, Paper A.
Kunz, K. S., and Moran, J. H., 1958, Some effects of formation anisotropy on resistivity measurements in boreholes: Geophysics, **23**, 770–794.
Maillet, R., and Doll, H. G., 1932, Théorème relatif aux millieux electriquement anisotropes et ses applications à la prospection electrique en courant continu: Erganzungshefte für Angewandte Geophysik, **3**, 109–124.
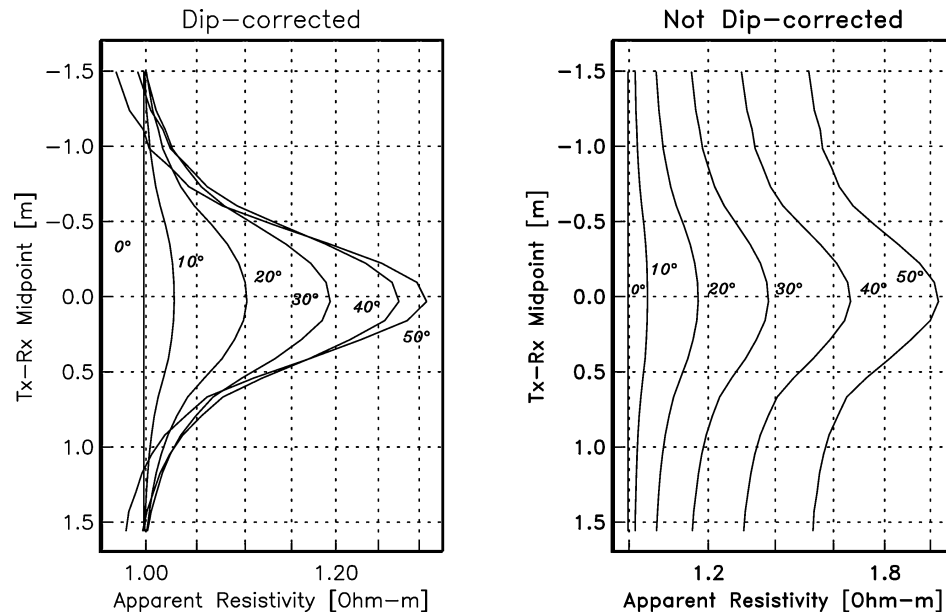
FIG. 10. The 2C–40 apparent resistivity curves (right) across a bed boundary in a symmetrically crossbedded formation (see Figure 9). The bed boundary is located at 0.0 on the vertical axis. Shown are the results for six cases of symmetrically dipping laminae with dip angle θ ranging from 0° to 50°. Shown on the left is a dip-corrected curve, where logging points in the set of curves shown on the right are scaled by a factor of $\cos\theta$, where θ is taken at the midpoint between the transmitter (Tx) and receiver (Rx) coils.
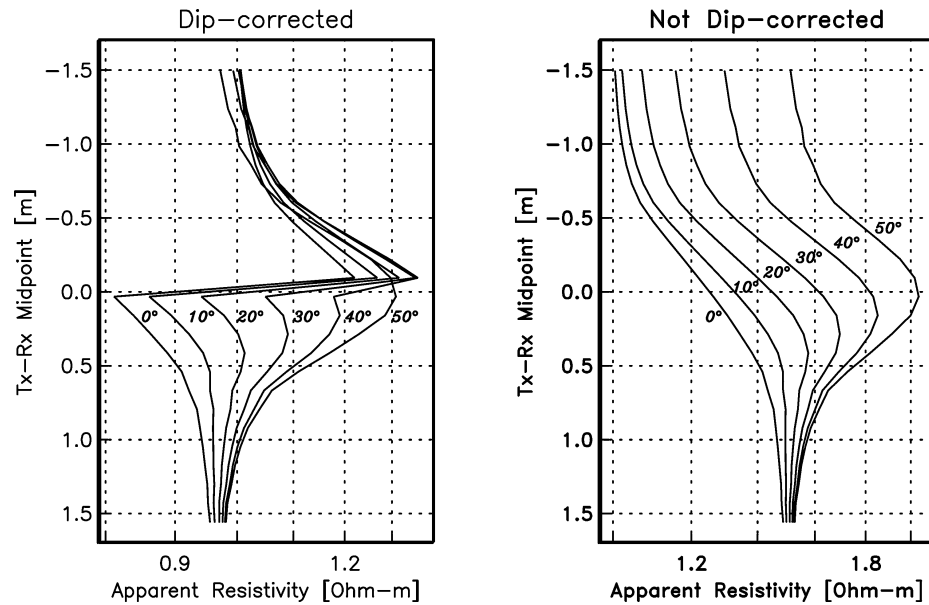

FIG. 11. The 2C–40 apparent resistivity curves (right) across a bed boundary in an asymmetrically crossbedded formation. The bed boundary is located at 0.0 on the vertical axis. Shown are the results for six cases where the orientation of the laminations in the lower bed remains fixed at $\theta = 50°$, while the laminations in the upper bed vary by an angle $\theta = 0°, 10°, \ldots, 50°$. Note the presence of polarization horns at $\sim$0.2 on the vertical axis of the dip-corrected results.

Moran, J. H., and Gianzero, S., 1979, Effects of formation anisotropy on resistivity-logging measurements: Geophysics, **44**, 1266–1286.

Moran, J. H., and Kunz, K. S., 1962, Basic theory of induction logging and application to study of two-coil sondes: Geophysics, **27**, 829–858.

Newman, G. A., and Alumbaugh, D. L., 1995, Frequency-domain modelling of airborne electromagnetic responses using staggered finite differences: Geophys. Prosp., **43**, 1021–1042.

——— 1999, Electromagnetic modeling and inverion on massively parallel computers, *in* Oristaglio, M., and Spies, B., Eds., Three dimensional electromagnetics: Soc. Expl. Geophys., 299–321.

——— 2002, Three-dimensional induction logging problems, part 2: A finite-difference solution: Geophysics, **67**, 000–000.

Onsager, L., 1931, Reciprocal relations in irreversible processes, I: Phys. Rev., **37**, 405–426.

Schön, J. H., Yu, L., Georgi, D. T., and Fanini, O., 2000, Aspects of multicomponent resistivity data and macroscopic resistivity anisotropy: 2000 Ann. Tech. Conf., Soc. Petr. Eng., Proceedings, paper SPE 62909.

Wang, T., and Hohmann, G. W., 1993, A finite difference time-domain solution for three-dimensional electromagnetic modeling: Geophysics, **58**, 797–809.

Weidelt, P., 1999, Three-dimensional conductivity models: Implications for electrical anisotropy, *in* Oristaglio, M., and Spies, B., Eds., Three-dimensional electromagnetics: Soc. Expl. Geophys., 119–137.

Yee, K. S., 1966, Numerical solution of initial boundary value problems involving Maxwell's equations in isotropic media: IEEE Trans. Ant. Prop., **14**, 302–307.

APPENDIX

FINITE-DIFFERENCE EQUATIONS

Following Newman and Alumbaugh (1995), a 13-point centered finite-difference stencil (Figure 2) is used to approximate the curl–curl operator in equation (5). Combining this with the conductivity averaging scheme described in this paper and assuming negligible displacement current effects, a set of linear equations for the x-, y-, and z-directed source terms in equation (5) are expressed as

$$
\left[E'_x\left(i+\tfrac{1}{2},j,k\right)-E'_x\left(i+\tfrac{1}{2},j-1,k\right)\right]\Big/\Delta^y_{j-1}\Delta^y_{j-\frac{1}{2}}+\left[E'_x\left(i+\tfrac{1}{2},j,k\right)-E'_x\left(i+\tfrac{1}{2},j+1,k\right)\right]\Big/\Delta^y_j\Delta^y_{j-\frac{1}{2}}
$$

$$
+\left[E'_x\left(i+\tfrac{1}{2},j,k-1\right)-E'_x\left(i+\tfrac{1}{2},j,k\right)\right]\Big/\Delta^z_{k-1}\Delta^z_{k-\frac{1}{2}}+\left[E'_x\left(i+\tfrac{1}{2},j,k\right)-E'_x\left(i+\tfrac{1}{2},j,k+1\right)\right]\Big/\Delta^z_k\Delta^z_{k-\frac{1}{2}}
$$

$$
+\left[E'_y\left(i,j-\tfrac{1}{2},k\right)-E'_y\left(i+1,j-\tfrac{1}{2},k\right)+E'_y\left(i+1,j+\tfrac{1}{2},k\right)-E'_y\left(i,j+\tfrac{1}{2},k\right)\right]\Big/\Delta^x_i\Delta^y_{j-\frac{1}{2}}
$$

$$
+\left[E'_z\left(i,j,k-\tfrac{1}{2}\right)-E'_z\left(i+1,j,k-\tfrac{1}{2}\right)+E'_z\left(i+1,j,k+\tfrac{1}{2}\right)-E'_z\left(i,j,k+\tfrac{1}{2}\right)\right]\Big/\Delta^x_i\Delta^z_{k-\frac{1}{2}}
$$

$$
+\frac{E'_x(i+\tfrac{1}{2},j,k)}{\Delta^y_{j-\frac{1}{2}}\Delta^z_{k-\frac{1}{2}}}\left[\tfrac{1}{2}\Delta^z_{k-1}\left(\tfrac{1}{2}\Delta^y_{j-1}\sigma^{[i,j-1,k-1]}_{xx}+\tfrac{1}{2}\Delta^y_j\sigma^{[i,j,k-1]}_{xx}\right)+\tfrac{1}{2}\Delta^z_k\left(\tfrac{1}{2}\Delta^y_{j-1}\sigma^{[i,j-1,k]}_{xx}+\tfrac{1}{2}\Delta^y_j\sigma^{[i,j,k]}_{xx}\right)\right]
$$

$$
+\frac{1}{\Omega^x_{i,j,k}}\left[\frac{\left(E'_y(i,j-\tfrac{1}{2},k)+E'_y(i+1,j-\tfrac{1}{2},k)\right)}{2/\tilde\sigma_{xy}\left(i+\tfrac{1}{2},j-\tfrac{1}{2},k\right)}+\frac{\left(E'_y(i,j+\tfrac{1}{2},k)+E'_y(i+1,j+\tfrac{1}{2},k)\right)}{2/\tilde\sigma_{xy}\left(i+\tfrac{1}{2},j+\tfrac{1}{2},k\right)}\right]
$$

$$
+\frac{1}{\Omega^x_{i,j,k}}\left[\frac{\left(E'_z(i,j,k-\tfrac{1}{2})+E'_z(i+1,j,k-\tfrac{1}{2})\right)}{2/\tilde\sigma_{xz}\left(i+\tfrac{1}{2},j,k-\tfrac{1}{2}\right)}+\frac{\left(E'_z(i,j,k+\tfrac{1}{2})+E'_z(i+1,j,k+\tfrac{1}{2})\right)}{2/\tilde\sigma_{xz}\left(i+\tfrac{1}{2},j,k+\tfrac{1}{2}\right)}\right]
$$

$$
=-i\omega\mu_0\left[\bar\sigma\left(i+\tfrac{1}{2},j,k\right)-\mathbf{I}\sigma_0\right]E^0_x\left(i+\tfrac{1}{2},j,k\right),\tag{A-1}
$$

$$
\left[E'_y\left(i,j+\tfrac{1}{2},k\right)-E'_y\left(i,j+\tfrac{1}{2},k-1\right)\right]\Big/\Delta^z_{k-1}\Delta^z_{k-\frac{1}{2}}+\left[E'_y\left(i,j+\tfrac{1}{2},k\right)-E'_y\left(i,j+\tfrac{1}{2},k+1\right)\right]\Big/\Delta^z_k\Delta^z_{k-\frac{1}{2}}
$$

$$
+\left[E'_y\left(i,j+\tfrac{1}{2},k\right)-E'_y\left(i-1,j+\tfrac{1}{2},k\right)\right]\Big/\Delta^x_{i-1}\Delta^x_{i-\frac{1}{2}}+\left[E'_y\left(i,j+\tfrac{1}{2},k\right)-E'_y\left(i+1,j+\tfrac{1}{2},k\right)\right]\Big/\Delta^x_i\Delta^x_{i-\frac{1}{2}}
$$

$$
+\left[E'_x\left(i-\tfrac{1}{2},j,k\right)-E'_x\left(i-\tfrac{1}{2},j+1,k\right)+E'_x\left(i+\tfrac{1}{2},j+1,k\right)-E'_x\left(i+\tfrac{1}{2},j,k\right)\right]\Big/\Delta^x_{i-\frac{1}{2}}\Delta^y_j
$$

$$
+\left[E'_z\left(i,j,k-\tfrac{1}{2}\right)-E'_z\left(i,j+1,k-\tfrac{1}{2}\right)+E'_z\left(i,j+1,k+\tfrac{1}{2}\right)-E'_z\left(i,j,k+\tfrac{1}{2}\right)\right]\Big/\Delta^y_j\Delta^z_{k-\frac{1}{2}}
$$

$$
+\frac{E'_y(i,j+\tfrac{1}{2},k)}{\Delta^x_{i-\frac{1}{2}}\Delta^z_{k-\frac{1}{2}}}\left[\tfrac{1}{2}\Delta^z_{k-1}\left(\tfrac{1}{2}\Delta^x_{i-1}\sigma^{[i-1,j,k-1]}_{yy}+\tfrac{1}{2}\Delta^x_i\sigma^{[i,j,k-1]}_{yy}\right)+\tfrac{1}{2}\Delta^z_k\left(\tfrac{1}{2}\Delta^x_{i-1}\sigma^{[i-1,j,k]}_{yy}+\tfrac{1}{2}\Delta^x_i\sigma^{[i,j,k]}_{yy}\right)\right]
$$

$$
+\frac{1}{\Omega^y_{i,j,k}}\left[\frac{\left(E'_x(i-\tfrac{1}{2},j,k)+E'_x(i-\tfrac{1}{2},j+1,k)\right)}{2/\tilde\sigma_{xy}\left(i-\tfrac{1}{2},j+\tfrac{1}{2},k\right)}+\frac{\left(E'_x(i+\tfrac{1}{2},j,k)+E'_x(i+\tfrac{1}{2},j+1,k)\right)}{2/\tilde\sigma_{xy}\left(i+\tfrac{1}{2},j+\tfrac{1}{2},k\right)}\right]
$$

$$
+\frac{1}{\Omega^y_{i,j,k}}\left[\frac{\left(E'_z(i,j,k-\tfrac{1}{2})+E'_z(i,j+1,k-\tfrac{1}{2})\right)}{2/\tilde\sigma_{yz}\left(i,j+\tfrac{1}{2},k-\tfrac{1}{2}\right)}+\frac{\left(E'_z(i,j,k+\tfrac{1}{2})+E'_z(i,j+1,k+\tfrac{1}{2})\right)}{2/\tilde\sigma_{yz}\left(i,j+\tfrac{1}{2},k+\tfrac{1}{2}\right)}\right]
$$

$$
=-i\omega\mu_0\left[\bar\sigma\left(i,j+\tfrac{1}{2},k\right)-\mathbf{I}\sigma_0\right]E^0_y\left(i,j+\tfrac{1}{2},k\right),\tag{A-2}
$$

and

$$\left[E_z'\left(i, j, k + \frac{1}{2}\right) - E_z'\left(i - 1, j, k + \frac{1}{2}\right)\right] \bigg/ \Delta_{i-1}^x \Delta_{i-\frac{1}{2}}^x + \left[E_z'\left(i, j, k + \frac{1}{2}\right) - E_z'\left(i + 1, j, k + \frac{1}{2}\right)\right] \bigg/ \Delta_i^x \Delta_{i-\frac{1}{2}}^x$$

$$+ \left[E_z'\left(i, j, k + \frac{1}{2}\right) - E_z'\left(i, j - 1, k + \frac{1}{2}\right)\right] \bigg/ \Delta_{j-1}^y \Delta_{j-\frac{1}{2}}^y + \left[E_z'\left(i, j, k + \frac{1}{2}\right) - E_z'\left(i, j + 1, k + \frac{1}{2}\right)\right] \bigg/ \Delta_j^y \Delta_{j-\frac{1}{2}}^y$$

$$+ \left[E_x'\left(i - \frac{1}{2}, j, k\right) - E_x'\left(i - \frac{1}{2}, j, k + 1\right) + E_x'\left(i + \frac{1}{2}, j, k + 1\right) - E_x'\left(i + \frac{1}{2}, j, k\right)\right] \bigg/ \Delta_{i-\frac{1}{2}}^x \Delta_k^z$$

$$+ \left[E_y'\left(i, j - \frac{1}{2}, k\right) - E_y'\left(i, j - \frac{1}{2}, k + 1\right) + E_y'\left(i, j + \frac{1}{2}, k + 1\right) - E_y'\left(i, j + \frac{1}{2}, k\right)\right] \bigg/ \Delta_{j-\frac{1}{2}}^y \Delta_k^z$$

$$+ \frac{E_z'\left(i, j, k + \frac{1}{2}\right)}{\Delta_{i-\frac{1}{2}}^x \Delta_{j-\frac{1}{2}}^y}\left[\frac{1}{2}\Delta_{j-1}^y\left(\frac{1}{2}\Delta_{i-1}^x \sigma_{zz}^{[i-1,j-1,k]} + \frac{1}{2}\Delta_i^x \sigma_{zz}^{[i,j-1,k]}\right) + \frac{1}{2}\Delta_j^y\left(\frac{1}{2}\Delta_{i-1}^x \sigma_{zz}^{[i-1,j,k]} + \frac{1}{2}\Delta_i^x \sigma_{zz}^{[i,j,k]}\right)\right]$$

$$+ \frac{1}{\Omega_{i,j,k}^z}\left[\frac{\left(E_x'\left(i - \frac{1}{2}, j, k\right) + E_x'\left(i - \frac{1}{2}, j, k + 1\right)\right)}{2/\tilde{\sigma}_{xz}\left(i - \frac{1}{2}, j, k + \frac{1}{2}\right)} + \frac{\left(E_x'\left(i + \frac{1}{2}, j, k\right) + E_x'\left(i + \frac{1}{2}, j, k + 1\right)\right)}{2/\tilde{\sigma}_{xz}\left(i + \frac{1}{2}, j, k + \frac{1}{2}\right)}\right]$$

$$+ \frac{1}{\Omega_{i,j,k}^z}\left[\frac{\left(E_y'\left(i, j - \frac{1}{2}, k\right) + E_y'\left(i, j - \frac{1}{2}, k + 1\right)\right)}{2/\tilde{\sigma}_{yz}\left(i, j - \frac{1}{2}, k + \frac{1}{2}\right)} + \frac{\left(E_y'\left(i, j + \frac{1}{2}, k\right) + E_y'\left(i, j + \frac{1}{2}, k + 1\right)\right)}{2/\tilde{\sigma}_{yz}\left(i, j + \frac{1}{2}, k + \frac{1}{2}\right)}\right]$$

$$= -i\omega\mu_0\left[\tilde{\sigma}\left(i, j, k + \frac{1}{2}\right) - \mathbf{I}\sigma_0\right]E_z^0\left(i, j, k + \frac{1}{2}\right), \tag{A-3}$$

where $\Omega_{i,j,k}^x = \Delta_i^x \Delta_{j-\frac{1}{2}}^y \Delta_{k-\frac{1}{2}}^z$, $\Omega_{i,j,k}^y = \Delta_{i-\frac{1}{2}}^x \Delta_j^y \Delta_{k-\frac{1}{2}}^z$ and $\Omega_{i,j,k}^z = \Delta_{i-\frac{1}{2}}^x \Delta_{j-\frac{1}{2}}^y \Delta_k^z$. The remaining $\tilde{\sigma}_{yz}$ term is given by

$$\tilde{\sigma}_{yz}\left(\alpha, \beta + \frac{1}{2}, \gamma + \frac{1}{2}\right) = \Delta_\beta^y\left(\frac{1}{2}\Delta_\gamma^z\right)\left(\frac{1}{2}\Delta_{\alpha-1}^x \sigma_{yz}^{[\alpha-1,\beta,\gamma]} + \frac{1}{2}\Delta_\alpha^x \sigma_{yz}^{[\alpha,\beta,\gamma]}\right), \tag{A-4}$$

where $\tilde{\sigma}_{xy}$ and $\tilde{\sigma}_{xz}$ are already defined in equations (11) and (12), respectively. As noted in Newman and Alumbaugh (1995), multiplication of equation (A-1) by the volume scaling terms $\Omega_{i,j,k}^x$, equation (A-2) by $\Omega_{i,j,k}^y$, and equation (A-3) by $\Omega_{i,j,k}^z$ results in a symmetric coefficient matrix for the isotropic case. It is straightforward, although somewhat tedious, to demonstrate that this assertion also holds for the anisotropic case presented here.